Tropopause Evolution in a Rapidly Intensifying Tropical Cyclone: A Static Stability Budget Analysis

Patrick Duran* and John Molinari

University at Albany, State University of New York, Albany, NY

**Corresponding author address:* Department of Atmospheric and Environmental Sciences, University at Albany, State University of New York, 1400 Washington Avenue, Albany, NY.

E-mail: pduran2008@gmail.com

ABSTRACT

We have some cool results!

1. Introduction

After undergoing a remarkably rapid intensification (RI), Hurricane Patricia (2015) set a new record as the strongest tropical cyclone (TC) ever observed in the Western Hemisphere (Kimberlain et al. 2016; Rogers et al. 2017). High-altitude dropsonde observations taken during the Tropical Cyclone Intensity (TCI) experiment captured this RI in unprecedented detail (Doyle et al. 2017). These observations revealed remarkable changes in the structure of the cold-point tropopause and upper-level static stability as the storm intensified (Duran and Molinari 2018).

At tropical storm intensity, shortly before RI commenced, a strong inversion layer existed just above Patricia's cold-point tropopause, which was located near 17.2 km. During the first half of the RI period, this inversion layer weakened throughout Patricia's inner core, with the weakening most pronounced over the developing eye. By the time the storm reached its maximum intensity, the inversion layer over the eye had disappeared almost completely, which was accompanied by an increase in the tropopause height to a level at or above the highest-available dropsonde data point (18.3 km) at two locations. Meanwhile over the eyewall region, the static stability re-strengthened and the tropopause was limited to a level at or below 17.5 km. The mechanisms that led to these changes in upper-level static stability and tropopause height are the subject of the current paper.

Despite the importance of tropopause-layer thermodynamics in theoretical models of hurricanes (Emanuel and Rotunno 2011; Emanuel 2012), few papers have examined the upper-tropospheric evolution of TCs. Komaromi and Doyle (2017) found that stronger TCs tended to have a higher and warmer tropopause over their inner core than weaker TCs. Their results are consistent with the evolution observed over the inner core of Hurricane Patricia, in which the tropopause height increased and the tropopause temperature warmed throughout RI (Duran and Molinari 2018). The simulations of Ohno and Satoh (2015) suggested that the development of an upper-level warm core within the eye acted to decrease the static stability near the tropopause. Although the mechanisms that drive this static stability evolution have not been examined explicitly, the potential temperature (θ) budget analysis of Stern and Zhang (2013) examined the development of the TC warm core. They found that radial and vertical advection both play important roles in warm core development throughout RI, with subgrid-scale diffusion becoming particularly important during the later stage of RI.

The analysis herein is based upon that of Stern and Zhang (2013), except using a static stability budget similar to that of Kepert et al. (2016) rather than a θ budget.

2. Model Setup

The numerical simulations were performed using version 19.4 of Cloud Model 1 (CM1) described in Bryan and Rotunno (2009). The equations of motion were integrated on a 3000-km-wide, 30-km-deep axisymmetric grid with 1-km horizontal and 250-m vertical grid spacing. The computations were performed on an f-plane at 15°N latitude, over a sea surface with constant temperature of 30.5°C, which matches that observed near Hurricane Patricia (2015; Kimberlain et al. 2016). Horizontal turbulence was parameterized using the Smagorinsky scheme described in Bryan and Rotunno (2009, pg. 1773), with a prescribed mixing length that varied linearly from 100 m at a surface pressure of 1015 hPa to 1000 m at a surface pressure of 900 hPa. This formulation allows for realistically-large horizontal mixing lengths near the hurricane's inner core, consistent with the results of Bryan (2012), while not over-representing horizontal turbulence in convection at outer radii. Vertical turbulence was parameterized using the formulation of Markowski and Bryan (2016, their Eq. 6), using an asymptotic vertical mixing length of 100 m. A Rayleigh damping layer was applied outside of the 2900-km radius and above the 25-km level to prevent spurious gravity wave reflection at the model boundaries. Microphysical processes were parameterized using the Thompson et al. (2004) microphysics scheme and radiative heating tendencies were computed every two minutes using the Rapid Radiative Transfer Model for GCMs (RRTMG) longwave and shortwave schemes (Iacono et al. 2008). The initial temperature and humidity field was horizontally homogeneous and determined by averaging all Climate Forecast System Reanalysis (CFSR) grid points within 100 km of Patricia's center of circulation at 18 UTC 21 October 2015. The vortex described in Rotunno and Emanuel (1987, their Eq. 37) was used to initialize the wind field, setting all parameters equal to the values used therein.

Although hurricanes simulated in an axisymmetric framework tend to be more intense than those observed in nature, the intensity evolution of this simulation matches reasonably well with that observed in Hurricane Patricia. After an initial spin-up period of about 20 hours, the modeled storm (Fig.1, blue lines) began an RI period that lasted approximately 30 hours. After this RI, the storm continued to intensify more slowly until the maximum 10-m wind speed reached 89 m s^{-1} and the minimum sea-level pressure reached its minimum of 846 mb, 81 hours into the simulation. Hurricane Patricia (red stars) exhibited a similar intensity evolution, with an RI period leading to a maximum 10-m wind speed of 95 m s^{-1} and a minimum sea-level pressure of 872 hPa. Despite the limitations of the axisymmetric framework, the extraordinary intensity of Hurricane Patricia and the rapidity of its intensification makes Patricia a particularly good candidate for axisymmetric analysis.

3. Budget Computation

The static stability can be expressed as the squared Brunt Väisälä frequency:

$$N_m^2 = \frac{g}{T}\left(\frac{\partial T}{\partial z} + \Gamma_m\right)\left(1 + \frac{T}{R_d/R_v + q_s}\frac{\partial q_s}{\partial T}\right) - \frac{g}{1+q_t}\frac{\partial q_t}{\partial z}, \tag{1}$$

where g is gravitational acceleration, T is temperature, R_d and R_v are the gas constants of dry air and water vapor, respectively, q_s is the saturation mixing ratio, q_t is the total condensate mixing ratio, and Γ_m is the moist-adiabatic lapse rate:

$$\Gamma_m = g(1+q_t)\left(\frac{1+L_v q_s/R_d T}{c_{pm}+L_v \partial q_s/\partial T}\right), \tag{2}$$

where L_v is the latent heat of vaporization and c_{pm} is the specific heat of moist air at constant pressure. In the tropopause layer, q_s, $\partial q_s/\partial T$, and $\partial q_t/\partial z$ approach zero. In this limiting case, Eq. 1 reduces to:

$$N^2 = \frac{g}{\theta}\frac{\partial \theta}{\partial z}, \tag{3}$$

where θ is the potential temperature.

To compute N^2, CM1 uses Eq.1 in saturated environments and Eq. 3 in sub-saturated environments. For simplicity, however, only Eq. 3 will be employed for the budget computations herein[1].

Taking the time derivative of Eq. 3 yields the static stability tendency:

$$\frac{\partial N^2}{\partial t} = \frac{g}{\theta}\frac{\partial}{\partial z}\frac{\partial \theta}{\partial t} - \frac{g}{\theta^2}\frac{\partial \theta}{\partial z}\frac{\partial \theta}{\partial t}, \tag{4}$$

where the potential temperature tendency, $\partial\theta/\partial t$, can be written:

$$\frac{\partial \theta}{\partial t} = HADV + VADV + HTURB + VTURB + MP + RAD + DISS \tag{5}$$

Each term on the right-hand side of Eq. 5 represents a θ budget variable, each of which is output directly by the model every minute. HADV and VADV are the radial and vertical advective tendencies, HTURB and VTURB are the radial and vertical tendencies from the turbulence parameterization, MP is the tendency from the microphysics scheme, RAD is the tendency from the radiation scheme, and DISS is the tendency due to turbulent dissipation. This equation neglects Rayleigh damping, since this term is zero everywhere below 25 km, and the analysis domain does

[1]The validity of this approximation will be substantiated later in this section.

not extend to that level. Each term in Eq. 5 is substituted for $\partial\theta/\partial t$ in Eq. 4, yielding the contribution of each budget term to the static stability tendency. These terms are summed, yielding an instantaneous ”budget change” in N^2 every minute. The budget changes are then averaged over 24-hour periods and compared to the total model change in N^2 over that same time period, i.e.:

$$\Delta N^2_{budget} = \frac{1}{\delta t} \sum_{t=t_0}^{t_0+\delta t} \left. \frac{\partial N^2}{\partial t} \right|_t \tag{6}$$

$$\Delta N^2_{model} = N^2_{t_0+\delta t} - N^2_{t_0} \tag{7}$$

$$Residual = \Delta N^2_{model} - \Delta N^2_{budget} \tag{8}$$

where t_0 is an initial time and δt is 24 hours.

Eqs. 6-8 are plotted for four consecutive 24-hour periods in Fig. 2. For this and all subsequent radial-vertical cross sections, a 1-2-1 smoother is applied once in the radial direction to eliminate $2\Delta r$ noise that appears in some of the raw model output and calculated fields. The left column of Fig. 2 depicts the model changes (Eq. 7), the center column depicts the budget changes (Eq. 6), and the right column depicts the residuals (Eq. 8). In every 24-hour period, the budget changes are nearly identical to the model changes, which is reflected in the near-zero residuals in the right column. This indicates that the budget accurately represents the model variability, which implies that the neglect of moisture in the budget computation introduces negligible error within the anaysis domain[2].

In the tropopause layer, some of the budget terms are small enough to be ignored. To determine which of the budget terms are most important, a time series of the contribution of each of the budget terms in Eq. 5 to the tropopause-layer static stability tendency is plotted in Fig. 4. For this figure, each of the budget terms is computed using the method described in Section 3, except with

[2]This is not the case in the lower- and mid-troposphere, where the residual actually exceeds the budget variability in many places, likely due to the neglect of moisture; thus we limit this analysis to the upper troposphere and lower stratosphere.

1-hour averaging intervals instead of 24-hour intervals. The absolute values of these tendencies are then averaged over a radius-height domain surrounding the tropopause and plotted as a time series[3]. Advection (Fig. 4, red line) plays an important role in the mean tropopause-layer static stability tendency at all times, and vertical turbulence (Fig. 4, blue line) and radiation (Fig. 4, dark green line) also contribute significantly. Although the contribution from horizontal turbulence (Fig. 4, purple line) becomes more important after 48 hours, it is confined to a very small region immediately surrounding the eyewall tangential velocity maximum (not shown), and is negligible throughout the rest of the tropopause layer. The remaining two processes - microphysics and dissipative heating (Fig. 4, orange and light green lines, respectively) - lie atop one another near zero. These time series indicate that, at all times, three budget terms dominate the tropopause-layer static stability tendency: advection, vertical turbulence, and radiation. Variations in the magnitude and spatial structure of these terms drive the static stability changes depicted in Fig. 2; subsequent sections will focus on these variations and what causes them.

4. Results

a. Static stability evolution

The average N^2 over the first day of the simulation (Fig. 3a) indicates the presence of a weak static stability maximum just above the cold-point tropopause. Over the subsequent 24 hours, during the RI period, the static stability within and above this layer decreased near the storm center (Fig. 3b). This decreasing N^2 corresponded to an increase in the tropopause height within the developing eye, maximized at the storm center. Outside of the eye, meanwhile, the tropopause

[3]It will be seeen in subsequent figures that each of the terms contributes both positively and negatively to the N^2 tendency within the analysis domain. Thus, taking an average over the domain tends to wash out the positive and negative contributions. To circumvent this problem, the absolute value of each of the terms is averaged.

height decresed over the eyewall region (25-60-km radius) and increased only slightly outside of the 60-km radius. In this outer region, the N^2 maximum just above the tropopause strengthened during RI. These trends continued as the storm's intensity leveled off in the 48-72-hour period (Fig. 3c). The tropopause height increased to nearly 21 km at the storm center and sloped sharply downward to 16.3 km on the inner edge of the eyewall, near the 30 km radius. Static stability outside of the eye, meanwhile, continued to increase just above the cold-point tropopause. This N^2 evolution closely follows that observed in Hurricane Patricia (2015; Duran and Molinari 2018). The mechanisms that led to these static stability changes will be investigated in the subsequent sections.

b. Static stability budget analysis

(i) 0-24 hours The weakening of the lower-stratospheric static stability maximum during the initial spin-up period is reflected in the total N^2 budget change over this time (Fig. 5a). The 17-18-km layer was characterized by decreasing N^2 (purple shading), maximizing at the storm center. The layer immediately below the tropopause, meanwhile, saw strengthening N^2 during this time period. Although these tendencies extended out to the 200-km radius, they were particularly pronounced at innermost radii. A comparison of the contributions of advection (Fig. 5b), vertical turbulence (Fig. 5c), and radiation (Fig. 5d) reveals that advection is primarily responsible for the change in static stability during this period. Although vertical turbulence acts in opposition to advection (i.e. it acts to stabilize regions that advection acts to destabilize), the magnitude of the advective tendencies is larger, particularly at the innermost radii. The sum of advection and vertical turbulence (Fig. 5e) almost exactly replicates the static stability tendencies above 17 km. Radiative tendencies (Fig. 5d) act to destabilize the layer below about 16 km and stabilize the

layer between 16 and 17 km. The sum of advection, vertical turbulence, and radiation (Fig. 5f) reproduces the total change in N^2 almost exactly.

...Explain this in the context of radial and vertical velocities... ...See Stern and Zhang, Page 84, Section 3d... ...Add mention of total condensate and radiative heating tendencies as it relates to statbility tendency due to rad...

(ii) 24-48 hours During the RI period within the eye, N^2 generally decreased above 16 km and increased below (Fig. 6a). These tendencies at the innermost radii were driven almost entirely by advection (Fig. 6b); vertical turbulence (Fig. 6c) and radiation (Fig. 6d) contributed negligibly to the static stability tendencies in this region. Outside of the eye, meanwhile, the N^2 evolution exhibited alternating layers of positive and negative tendencies. Near and above 18 km existed an upward-sloping region of decreasing N^2 that extended out to the 180-km radius. In this region, neither vertical turbulence nor radiation exhibited negative N^2 tendencies; advection was the only forcing for destabilization. Immediately below this layer was a region of increasing N^2, which sloped upward from 17 km near the 30-km radius to just below 18 km outside of the 100 km radius. Advection and vertical turbulence both contributed to this positive N^2 tendency, with advection playing an important role below about 17.5 km and and turbulence playing an important role above. The sum of advection and turbulence (Fig. 6e) reveals two discontiguous regions of increasing N^2 rather than one contiguous region. The addition of radiation to these two terms, however, (Fig. 6f) provides the link between these two regions, indicating that radiation also plays a role in strengthening the stable layer just above the tropopause. Below 17 km, a horizontally-extensive layer of decreasing N^2 also was forced by a combination of advection, vertical turbulence, and radiation. The sum of advection and vertical turbulence accounts only for two isolated regions of decreasing N^2 in this layer, and actually forces stabilization in part of the region. For example, just

above 16 km in the 150-200-km radial band, the sum of advection and vertical turbulence forces an increase in N^2. Likewise, throughout most of the 30-60-km radial band in this layer, advection and vertical turbulence combine to force near-zero or positive N^2 tendencies. Radiative tendencies overcome this forcing for stabilization in both of these regions to produce the radially-extensive region of destabilization just below the tropopause.

TWO REGIONS WHERE Panel (f) differs from panel (a): 30-60 km radial band below 16 km, which is actually canceled out by a vertical gradient of latent heating, and the thin region of strong stabilization between 15-17.5 km near r=30 km, which is canceled out by horizontal turbulence.

(iii) 48-72 hours The third day of the simulation marked a dramatic change in the structure of the tropopause-layer static stability tendencies. During this time, static stability increased markedly in an upward-sloping region within the 30-60-km radial band (Fig. 7a), and also increased within the 16.75-17.5-km layer out to at least the 200-km radius. As this layer stabilized, the layer immediately below it destabilized in a broad region extending from 60-200 km. Examination of the contribution from total advection (Fig. 7b) reveals that advection no longer dominates the static stability tendencies. Instead, a combination of vertical turbulence (Fig. 7c) and radiation (Fig. 7d) overcomes the destabilizing influence of advection to create the layer of increasing static stability. Meanwhile, the destabilizing influence of vertical turbulence in a broad region below 17 km combines with a small region of destabilization due to radiation in the 50-120-km radial band combine to destabilize the layer below 16.5 km in the 50-200-km radial band. Comparing the sum of advection and vertical turbulence (Fig. 7e) to the sum of advection, vertical turbulence, and radiation (Fig. 7f) reveals that radiation plays a fundamental role in the re-strengthening of the lower-stratospheric stable layer during this time.

(iv) 72-96 hours

5. Discussion

Radiative heating and turbulence viscosity figures?

Discuss how turbulence increases the static stability in some regions –¿ vertical gradients of turblence intensity.

Dunion et al. speculate that the diurnal pulse only occurs in mature storms. Maybe the development of the near-tropopause stable layer could partially explain the reason for this.

Acknowledgments. We are indebted to George Bryan for his continued development and support of Cloud Model 1. We also thank Jeffrey Kepert, Robert Fovell, and Erika Navarro for helpful conversations related to this work. ADD GRANT NUMBER

References

Bryan, G. H., 2012: Effects of surface exchange coefficients and turbulence length scales on the intensity and structure of numerically simulated hurricanes. *Mon. Wea. Rev.*, **140**, 1125–1143.

Bryan, G. H., and R. Rotunno, 2009: The maximum intensity of tropical cyclones in axisymmetric numerical model simulations. *Mon. Wea. Rev.*, **137**, 1770–1789.

Doyle, J. D., and Coauthors, 2017: A view of tropical cyclones from above: The Tropical Cyclone Intensity (TCI) Experiment. *Bull. Amer. Meteor. Soc.*, **98**, 2113–2134.

Duran, P., and J. Molinari, 2018: Dramatic inner-core tropopause variability during the rapid intensification of Hurricane Patricia (2015). *Mon. Wea. Rev.*, **XXX**, XXX–XXX.

Emanuel, K., 2012: Self-stratification of tropical cyclone outflow. part ii: Implications for storm intensification. *J. Atmos. Sci.*, **69**, 988–996.

Emanuel, K., and R. Rotunno, 2011: Self-stratification of tropical cyclone outflow. part i: Implications for storm structure. *J. Atmos. Sci.*, **68**, 2236–2249.

Iacono, M. J., J. S. Delamere, E. J. Mlawer, M. W. Shephard, S. A. Clough, and W. D. Collins, 2008: Radiative forcing by long-lived greenhouse gases: Calculations with the AER radiative transfer models. *J. Geophys. Res.*, **113 (D13103)**.

Kepert, J. D., J. Schwendike, and H. Ramsay, 2016: Why is the tropical cyclone boundary layer not ”well mixed”? *J. Atmos. Sci.*, **73**, 957–973.

Kimberlain, T. B., E. S. Blake, and J. P. Cangialosi, 2016: Tropical cyclone report: Hurricane Patricia. National Hurricane Center. [Available online at www.nhc.noaa.gov].

Komaromi, W. A., and J. D. Doyle, 2017: Tropical cyclone outflow and warm core structure as revealed by HS3 dropsonde data. *Mon. Wea. Rev.*, **145**, 1339–1359.

Markowski, P. M., and G. H. Bryan, 2016: LES of laminar flow in the PBL: A potential problem for convective storm simulations. *Mon. Wea. Rev.*, **144**, 1841–1850.

Ohno, T., and M. Satoh, 2015: On the warm core of a tropical cyclone formed near the tropopause. *J. Atmos. Sci.*, **72**, 551–571.

Rogers, R. F., S. Aberson, M. M. Bell, D. J. Cecil, J. D. Doyle, J. Morgerman, L. K. Shay, and C. Velden, 2017: Re-writing the tropical record books: The extraordinary intensification of Hurricane Patricia (2015). *Bull. Amer. Meteor. Soc.*, **98**, 2091–2112.

Rotunno, R., and K. A. Emanuel, 1987: An air-sea interaction theory for tropical cyclones. Part II: Evolutionary study using a nonhydrostatic axisymmetric numerical model. *J. Atmos. Sci.*, **44**, 542–561.

Stern, D. P., and F. Zhang, 2013: How does the eye warm? part i: A potential temperature budget analysis of an idealized tropical cyclone. *J. Atmos. Sci.*, **70**, 73–89.

Thompson, G., R. M. Rasmussen, and K. Manning, 2004: Explicit forecasts of winter precipitation using an improved bulk microphysics scheme. Part I: Description and sensitivity analysis. *Mon. Wea. Rev.*, **132**, 519–542.

LIST OF FIGURES

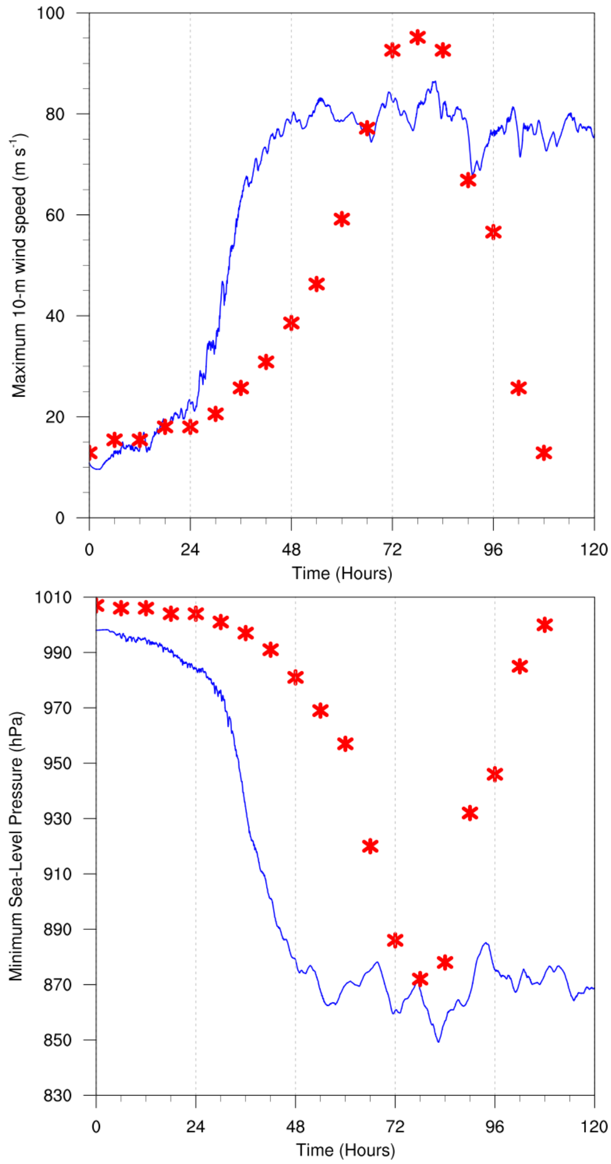

FIG. 1. The maximum 10-m wind speed (top panel; m s^{-1}) and minimum sea-level pressure (bottom panel; hPa) in the simulated storm (blue lines) and from Hurricane Patricia's best track (red stars).

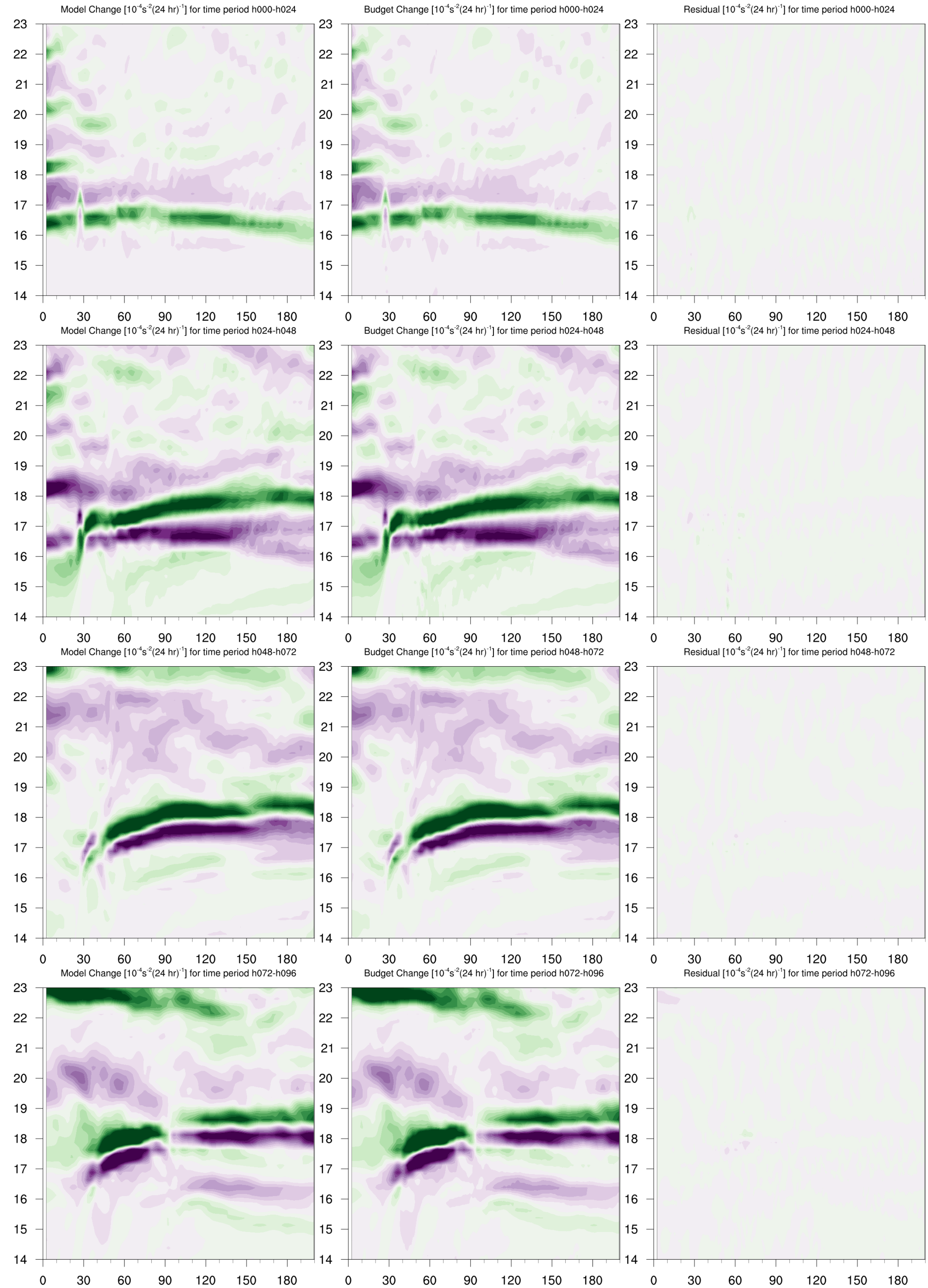

FIG. 2. Left panels: Twenty-four-hour changes in squared Brunt-Väisälä frequency (N^2; 10^{-4} s^{-2}) over (a)

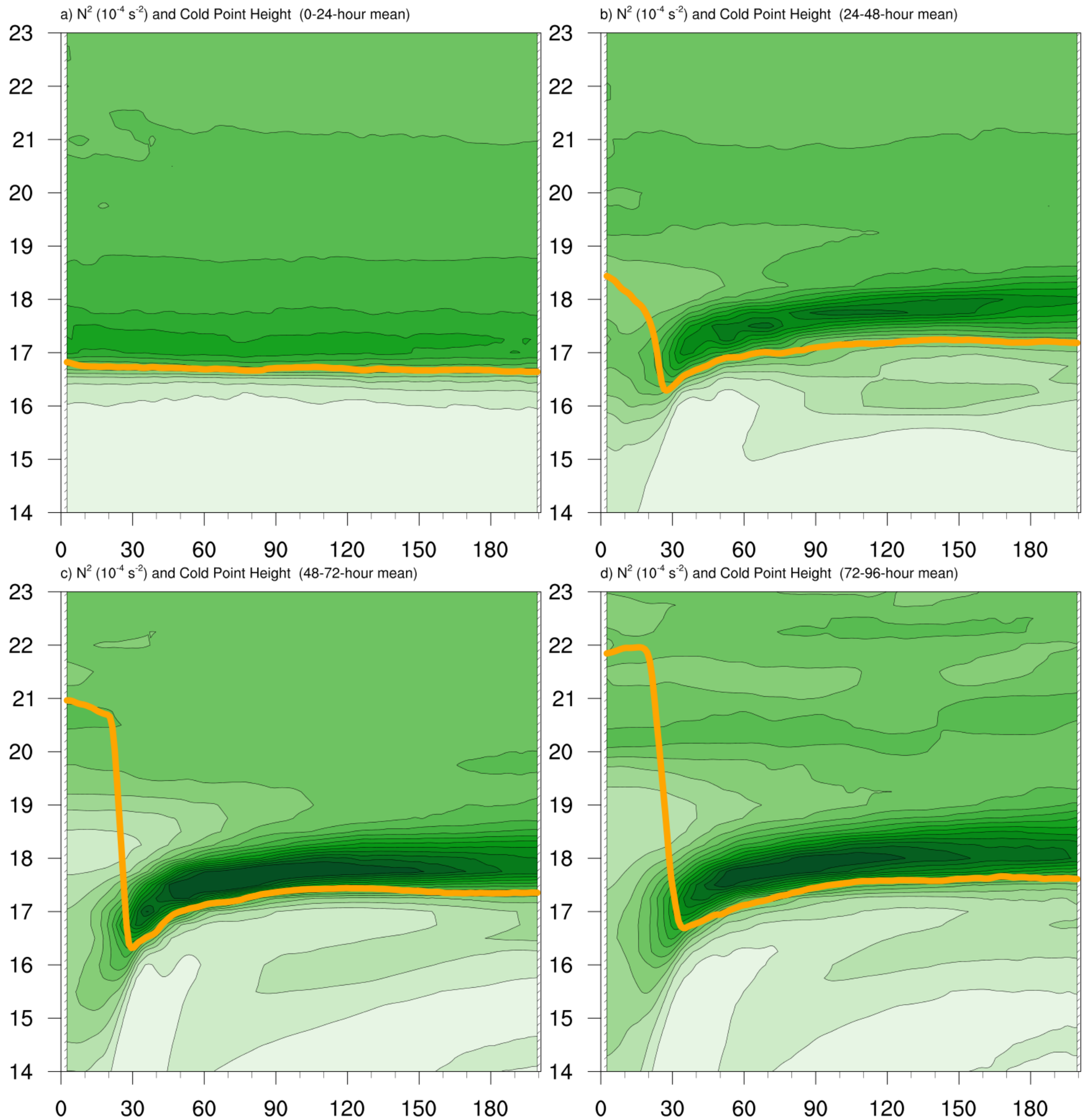

FIG. 3. Twenty-four-hour averages of squared Brunt-Väisälä frequency (10^{-4} s^{-2}) over the first four days of the simulation. Orange lines represent the cold-point tropopause determined by the mean temperature field over the same time periods.

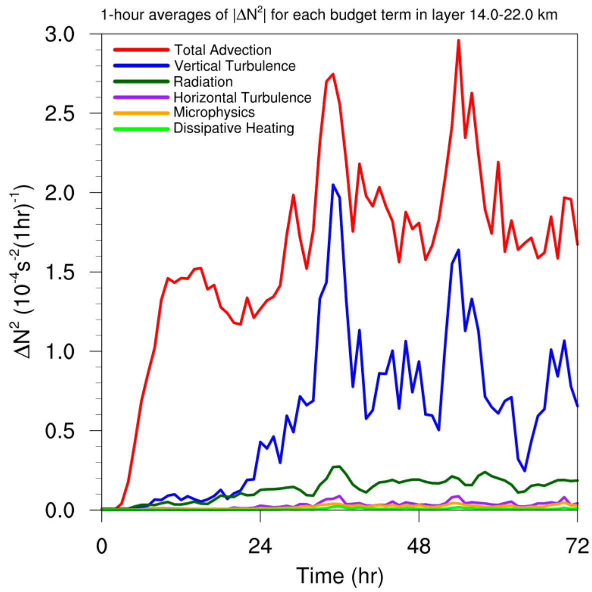

FIG. 4. Time series of the contribution of each of the budget terms to the time tendency of the squared Brunt-Väisälä frequency (N^2; 10^{-4} s^{-2}). For each budget term, the absolute value of the N^2 tendency is averaged temporally over 1-hour periods (using output every minute), and spatially in a region extending from 0 to 200 km radius and 14 to 21 km altitude.

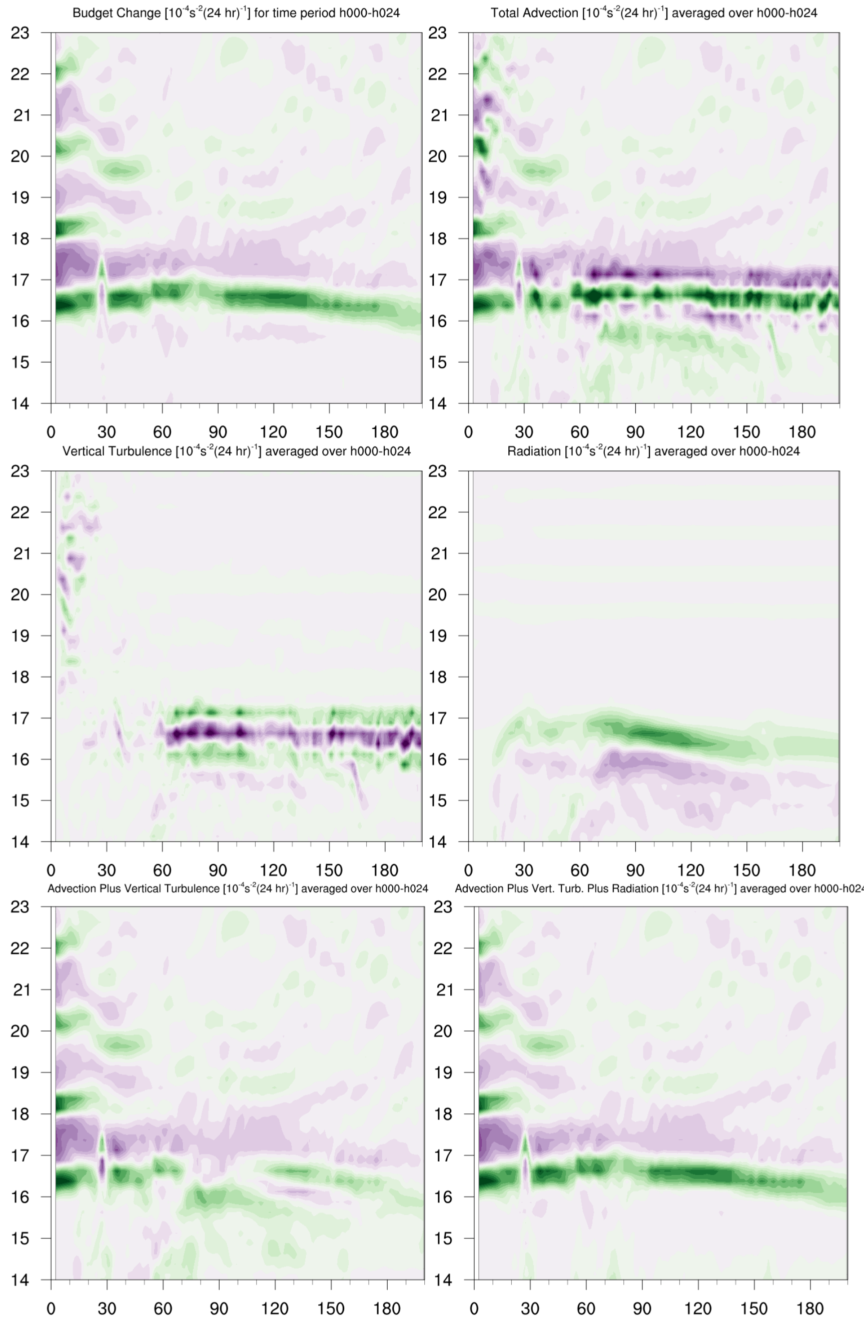

FIG. 5. (a) Total change in N^2 over the 0-24-hour period (10^{-4} s^{-2} $(24\ hr)^{-1}$) and the contributions to that change from (b) the sum of horizontal and vertical advection, (c) vertical turbulence, (d) longwave and shortwave radiation, (e) the sum of horizontal advection, vertical advection, and vertical turublence, and (f) the sum of horizontal advection, vertical advection, vertical turbulence, and longwave and shortwave radiation.

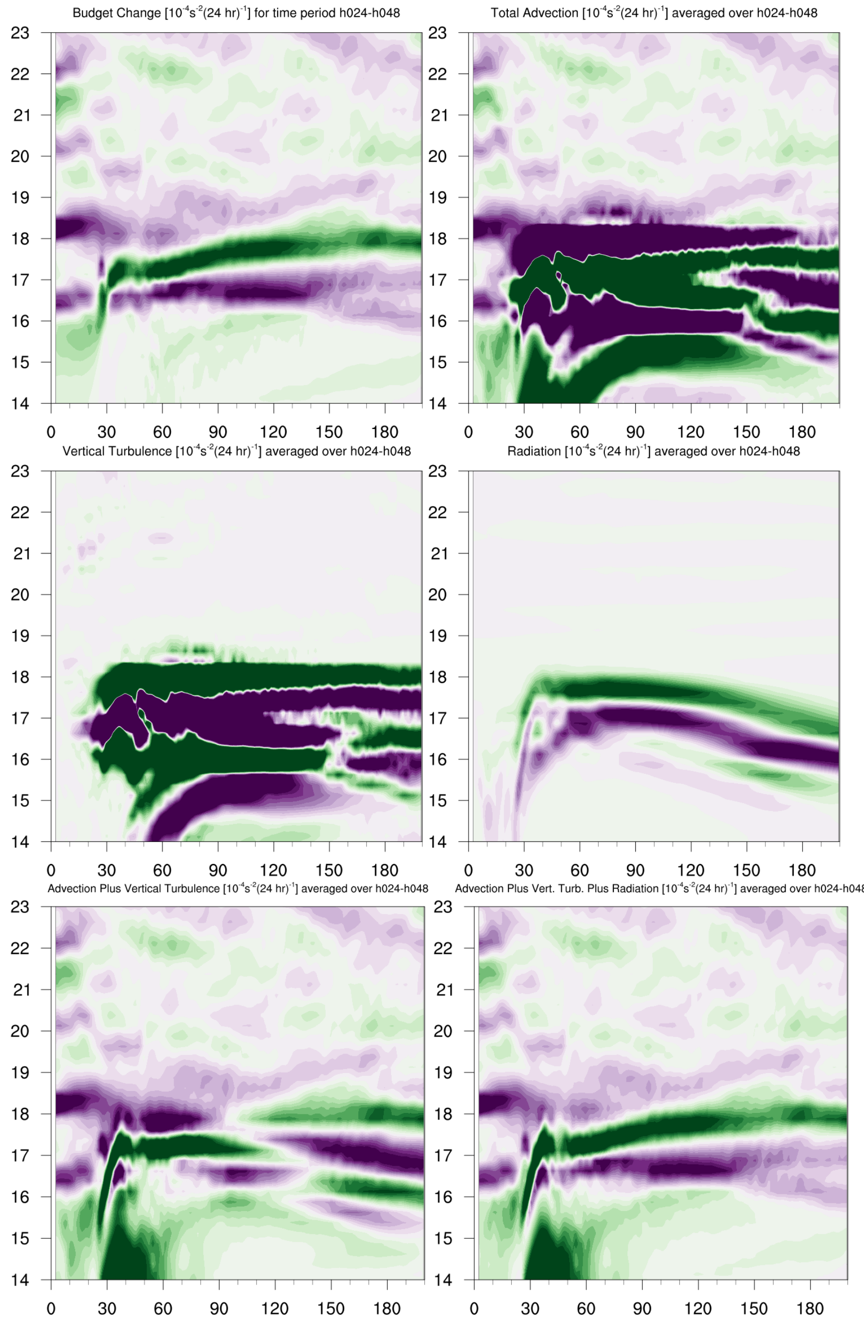

FIG. 6. As in Fig. 5, but for the 24-48-hour period.

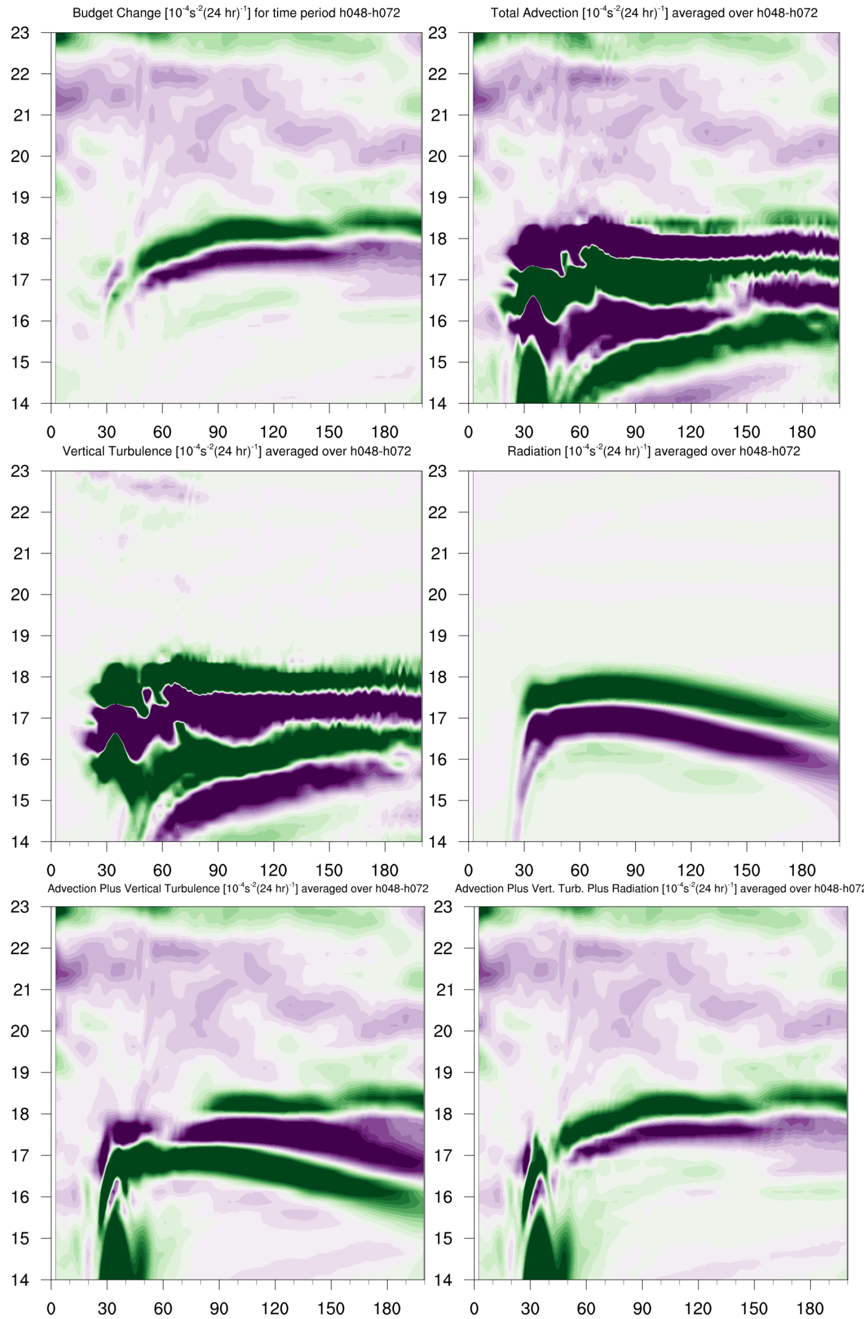

FIG. 7. As in Fig. 5, but for the 48-72-hour period.

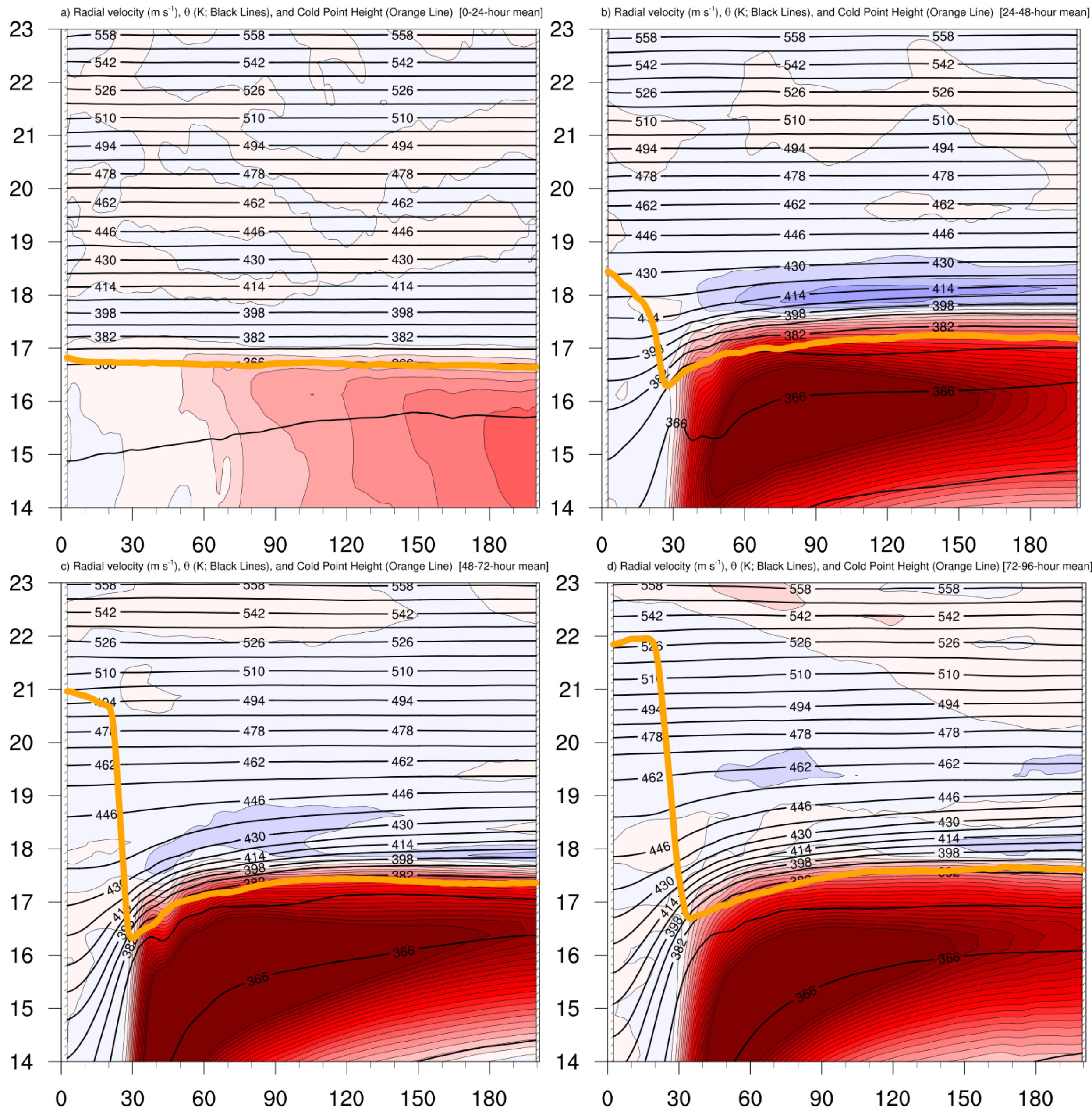

FIG. 8. Radial velocity (m s^{-1}; filled contours), potential temperature (K; thick black contours), and cold point tropopause height (orange lines) averaged over (a) 0-24 hours, (b) 24-48 hours, and (c) 48-72 hours.

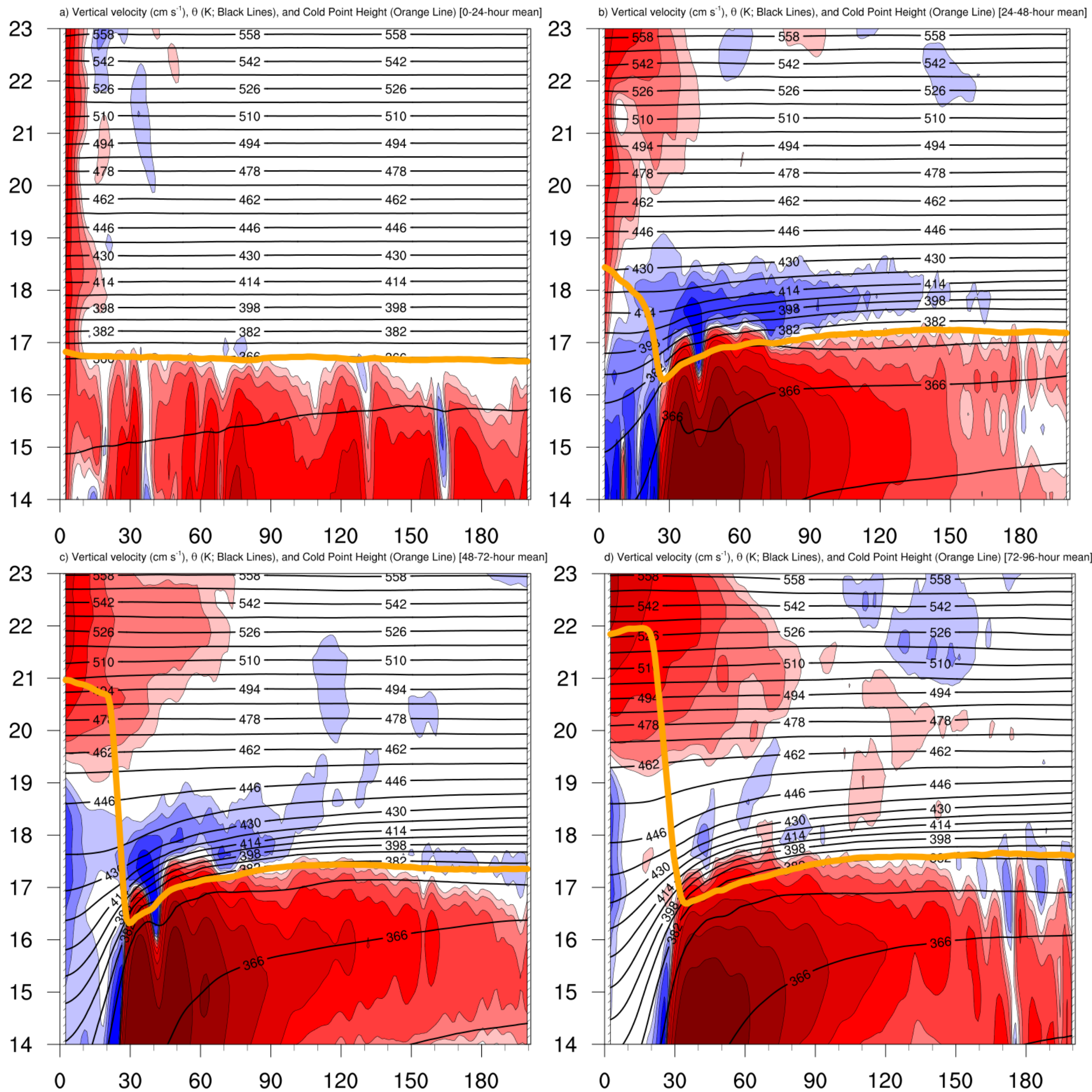

FIG. 9. Vertical velocity (cm s^{-1}; filled contours), potential temperature (K; thick black contours), and cold point tropopause height (orange lines) averaged over (a) 0-24 hours, (b) 24-48 hours, and (c) 48-72 hours.

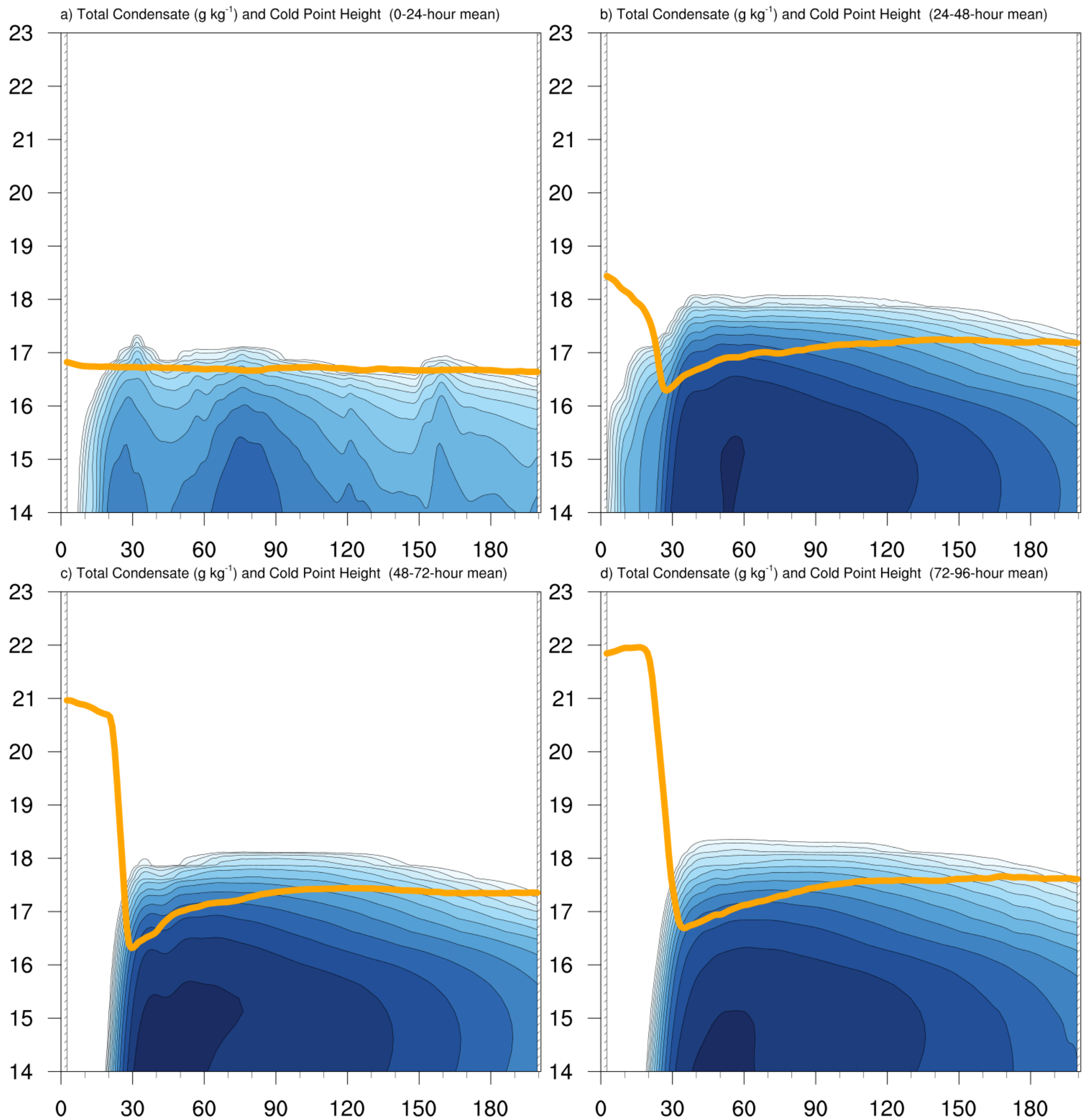

301 FIG. 10. Total condensate mixing ratio (g kg^{-1}) and cold point tropopause height (orange lines) averaged over

302 (a) 0-24 hours, (b) 24-48 hours, and (c) 48-72 hours.

figures/radten.png

FIG. 11. Radiative heating rate (K hr^{-1}) and cold point tropopause height (orange lines) averaged over (a) 0-24 hours, (b) 24-48 hours, and (c) 48-72 hours.

figures/khvten.png

FIG. 12. Vertical eddy diffusivity (m^2 s^{-2}; filled contours), cold point tropopause height (cyan lines), and radial velocity (m s^{-1}; thick black lines) averaged over (a) 0-24 hours, (b) 24-48 hours, and (c) 48-72 hours.